PNAS RESEARCH ARTICLE | PHYSICS

Atomistic twinning process with ultra-high shear in hexagonal close-packed crystals

Yang He[a], Dengke Chen[b], Chongmin Wang[c,1], Ting Zhu[b,1], Yuyang Wang[d], Bin Li[d,1], and Scott X. Mao[a,e,1]

Edited by Valeria Molinero, The University of Utah, Salt Lake City, UT; received February 26, 2026; accepted July 21, 2026

Twinning is a critical deformation mechanism that can significantly enhance the mechanical performance of materials. Predicting active twinning modes has long been a fundamental challenge. It is generally believed that active twinning modes should exhibit low to moderate shear strains to minimize the associated strain energy. Here, using in situ atomic-scale straining experiments, we identify an unconventional twinning mode in hexagonal close-packed (HCP) rhenium nanocrystals, characterized by an extraordinarily large shear strain of ~1.2, the highest reported for HCP crystals to date. Remarkably, this twinning process proceeds via pure lattice shear without the atomic shuffling typically required for conventional HCP twinning. Our results indicate that high stress states attainable in nanocrystals, together with favorable energetics, enable activation of this mode. This ultra-high-shear twinning mechanism holds significant potential for enhancing the formability and ductility of HCP metals.

hexagonal close-packed crystal | atomistic twinning | lattice shear

Significance

Our results demonstrate that extreme stress states accessible in nanocrystals, together with favorable energetic conditions, can activate deformation modes that are inaccessible in bulk materials and absent from existing twinning theories. This finding expands the known space of crystallographic twinning mechanisms and reveals a previously unrecognized route for accommodating large plastic strains in hexagonal close-packed (HCP) metals. More broadly, the identified ultra-high-shear twinning mechanism suggests opportunities for enhancing the ductility and formability of HCP materials through microstructural and size-scale design.

Twinning, along with dislocation slip, is a fundamental deformation mode of crystal deformation that enables the simultaneous enhancement of strength and ductility in materials ranging from metals to biominerals (1–4). Identifying the active twinning mode for the mechanical deformation of a material is therefore essential for understanding and tailoring its properties. Traditionally, a twinning mode is characterized by four crystallographic elements: the twinning plane K_1, the conjugate twinning plane K_2, the twinning shear direction η_1, and the conjugate twinning shear direction η_2 (Fig. 1*A*). It is generally accepted that the preferred twinning mode on a twinning plane involves a small to moderate shear, which minimizes the mismatch between the twin and matrix and, consequently, reduces the associated strain energy (5–7). Although this principle has been extensively validated in bulk materials, it remains largely untested in nanoscale crystals, particularly those with complex lattice structures containing multiple atoms per unit cell, where twinning involves not only lattice shear but also atomic shuffling (5, 8).

In principle, the deconfined geometry of nanocrystals truncates the shear strain field ahead of a growing twin tip (as schematically illustrated in Figs. 1 *B* and *C*), thereby reducing the energy barrier for twinning shear (9). In crystals with complex lattice structures, however, this effect has minimal influence on atomic shuffling, which does not contribute to macroscopic deformation. In addition, reducing crystal size enables the attainment of high stress levels (10), resulting in large resolved shear stresses on the twin plane along the twinning shear direction. This condition can significantly lower the energy barrier for twinning modes with large shear (11). Consequently, unconventional twinning modes with minimum atomic shuffling and large twinning shear may become energetically favorable in nanoscale crystals.

Here, using in situ high-resolution transmission electron microscopy (HRTEM) combined with advanced crystal manipulation techniques, we directly observed a twinning mode with atomic process in hexagonal close-packed (HCP) rhenium (Re) nanocrystals (Fig. 1*D*). In contrast to conventional expectations, this mode exhibits largest possible twinning shear along with minimum atomic shuffling. These findings demonstrate that active twinning in nanoscale crystals can fundamentally differ from that in their bulk counterparts.

Fig. 2 *A*–*D* show sequential HRTEM snapshots of a $\{11\bar{2}2\}$ twinning process in a $[10\bar{1}0]$-oriented HCP Re nanocrystal. This nanocrystal, free of preexisting defects, was fabricated inside the TEM (*Methods*). A tensile load was applied along the axial direction of approximately $[\bar{1}2\bar{1}6]$, generating a large, resolved shear stress on the $(1\bar{2}12)[1\bar{2}\bar{1}3]$ twinning system (Schmid factor ~0.495). Note that the Schmid factor is larger than those of competing twinning systems of $(1\bar{1}02)[1\bar{1}0\bar{1}]$ (Schmid factor ~0.411) and $(1\bar{2}11)[1\bar{2}\bar{1}6]$ (Schmid factor ~0.466). Twinning on the $(1\bar{2}12)$ plane was directly observed during deformation,

Author affiliations: [a]Department of Mechanical Engineering and Materials Science, University of Pittsburgh, Pittsburgh, PA 15261; [b]Woodruff School of Mechanical Engineering, Georgia Institute of Technology, Atlanta, GA 30332; [c]Environmental Molecular Sciences Laboratory, Pacific Northwest National Laboratory, Richland, WA 99352; [d]Department of Manufacturing Engineering, Iowa State University, Ames, IA 50011; and [e]School of Materials Engineering, Purdue University, West Lafayette, IN 47907

Author contributions: Y.H. and S.X.M. designed research; Y.H. and B.L. performed research; C.W. and B.L. contributed new reagents/analytic tools; Y.H., D.C., T.Z., and B.L. analyzed data; S.X.M. revised the paper; and Y.H., T.Z., Y.W., and B.L. wrote the paper.

The authors declare no competing interest.

This article is a PNAS Direct Submission.

[1]To whom correspondence may be addressed. Email: chongmin.wang@pnnl.gov, ting.zhu@me.gatech.edu, binl@iastate.edu, or mao217@purdue.edu.

This article contains supporting information online at https://www.pnas.org/lookup/suppl/doi:10.1073/pnas.2607072123/-/DCSupplemental.

Published August 19, 2026.

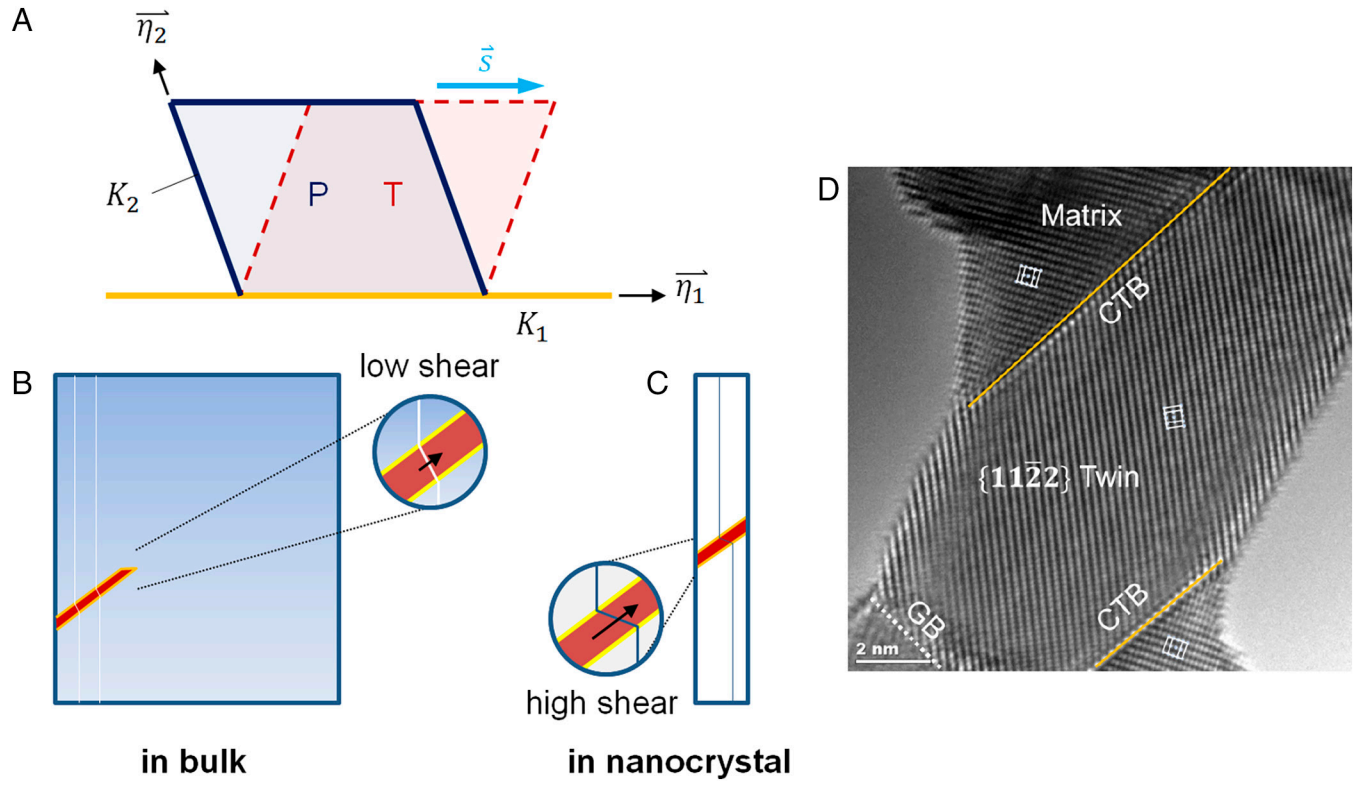

Fig. 1. $\{11\bar{2}2\}$ twinning in an HCP nanocrystal. (*A*) Schematic illustrating the elements of twinning. (*B* and *C*) Conceptual diagrams showing the size-dependent twinning behavior in bulk (*B*) and nanoscale (*C*) HCP crystals. (*D*) Representative HRTEM image capturing the formation of a $\{11\bar{2}2\}$ twin in a Re nanocrystal during in situ tensile deformation.

as evidenced by the lattice pattern with mirror symmetry across coherent twin boundaries (CTBs) in Figs. 1*D* and 2*B*.

The observed twinning mode is distinct from the conventional $\{11\bar{2}2\}$ twinning reported in bulk HCP crystals (9, 12, 13). First, the observed $\{11\bar{2}2\}$ twinning produces a tension twin, accommodating applied tensile strain along the <***c***> axis of the HCP crystal. In contrast, the conventional $\{11\bar{2}2\}$ twinning creates a contraction twin. Second, K_2 plane of the observed twinning is the (0001) basal plane, rather than the $\{11\bar{2}\bar{4}\}$ plane associated with conventional $\{11\bar{2}2\}$ twinning. This identification is supported by our in-situ observations (Fig. 2 *E* and *F*), which show that the basal surface facet of the parent crystal transformed into the basal surface facet of the twin, indicating that (0001) serves as the K_2 plane. Additionally, by tracking atomic movements during the twinning process, we found that the matrix $(\bar{1}2\bar{1}4)$ plane transformed to the $(1\bar{2}18)$ plane in the twin, confirming that the $\{11\bar{2}\bar{4}\}$ plane is not the conjugate twining plane in this mode. Third, based on the twinning-induced surface tilt (Fig. 2 *E* and *F*), the twinning shear strain is estimated to be ~1.2, substantially larger than the ~0.25 shear strain associated with the conventional $\{11\bar{2}2\}$ twinning in Re (5, 12, 14). This exceptionally large twinning shear is further corroborated by direct measurements of atom-columns movements from sequential in situ HRTEM images (*SI Appendix*, Fig. S1).

We used the dichromatic map (Fig. 2*G*) to identify the twinning elements of the observed mode. There are six possible twinning modes on the $\{11\bar{2}2\}$ plane. Based on the observed K_2 plane and the measured twinning shear, the twinning elements are determined as $K_1\{11\bar{2}2\}$, K_2 (0001), $\eta_1\langle 11\bar{2}3\rangle$, and $\eta_2\langle 11\bar{2}0\rangle$. The theoretical shear strain for this mode is $2/\gamma$ (γ=*c*/*a*; *c* and *a* are lattice constants), giving a value of about 1.2—matching the experimental measurement. This twinning mode requires no atomic shuffling, consistent with the minimal internal atomic displacements within unit cells observed. An additional unique feature of this twinning mode comes from the behavior of twinning dislocations (TDs). Since the lattice repeats every two units along η_2, the TD is expected to produce a step height of one $\{11\bar{2}2\}$ layer (5, 15). This is exactly what we observed: in Fig. 2 *C* and *D*, a TD with a single-layer step moves from the upper-right to the lower-left, adding one $\{11\bar{2}2\}$ layer to the twin. Such TDs are also responsible for the layer-by-layer growth of the $\{11\bar{2}2\}$ twin during twinning and detwinning (*SI Appendix*, Fig. S1). In contrast, conventional $\{11\bar{2}2\}$ twinning involves TDs with three-layer steps. The single-layer TD we observed would be unstable in any other $\{11\bar{2}2\}$ twinning modes, as it would create mismatch twin boundaries, further confirming the uniqueness of this mode.

The observed twinning mode has not been previously reported in experiments and is generally considered unlikely due to its exceptionally large twinning shear. More favorable twinning modes on the $\{10\bar{1}2\}$ and $\{11\bar{2}1\}$ planes are typically available to accommodate applied tensile strain along the <***c***> axis (16–18). This raises a question: why does this high-shear twinning mode becomes active, prevailing over conventional low and moderate shear modes on the $\{10\bar{1}2\}$ and $\{11\bar{2}1\}$ planes? While the high stress levels attainable in nanoscale crystals likely play a critical role (10, 19, 20), we further evaluate the observed twinning shear mode by comparing its energetics with those of competing twinning modes on the same twinning plane.

As shown in Fig. 2, where the possible K_2 planes are plotted, the observed b_1 TD is the least plausible according to classical twinning theory that favors small twinning shear (5). This TD directly shears

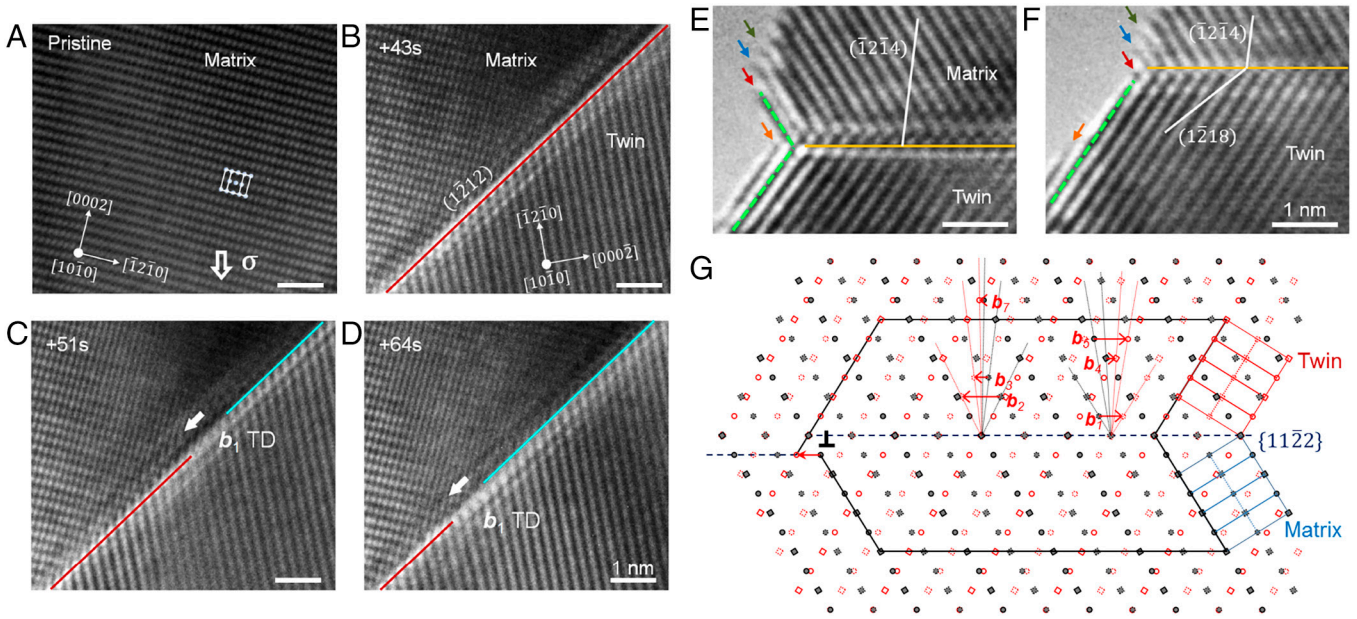

Fig. 2. In situ atomic-resolution observation of $\{11\bar{2}2\}$ twinning in a Re nanocrystal during in situ tensile deformation. (*A*–*D*) Sequential HRTEM snapshots showing the formation of a $\{11\bar{2}2\}$ twin. The inset in (*A*) shows a schematic of the HCP unit cell. The arrow in (*C* and *D*) indicates the gliding direction of a b_1 twinning dislocation (TD). (*E* and *F*) Sequential HRTEM images highlighting the evolution of the surface facet during twinning. Color-coded arrows mark individual basal planes; the green dashed line outlines the basal surface facet; the yellow line traces the $(1\bar{2}12)$ twin boundary; and white lines indicate the corresponding matrix plane $(\bar{1}2\bar{1}4)$. (*G*) Dichromatic map illustrating the $\{11\bar{2}2\}$ twinning system, showing all topologically possible K_2 planes (dotted lines) and the Burgers vectors of candidate twinning dislocations (red arrows). The K_2 planes corresponding to b_1, b_2, b_3, b_4, b_5, b_7 modes are (0001), $\{11\bar{2}2\}$, $\{11\bar{2}4\}$, $\{11\bar{2}6\}$, $\{11\bar{2}8\}$, $\{11\bar{2}5\}$, respectively. The black and red dotted lines indicate K_2 planes of the matrix and twin, respectively. Black lines indicate the Frank loop for the twinning dislocation. The observed twinning mode follows the b_1 dislocation, which produces the largest twinning shear, while the conventional $\{11\bar{2}2\}$ twinning corresponds to b_3. [Scale bar in (*A*–*F*), 1 nm.]

all atoms in the parent lattice into twin positions without requiring additional atomic shuffles. In contrast, for all other twinning modes with different K_2 planes, substantial atomic shuffles are necessary to accomplish the twinning process. The magnitude and complexity of these shuffles depend strongly on the specific K_2 plane. In general, a smaller twinning shear is associated with more complex shuffling. Classical twinning theory predicts the $\{11\bar{2}4\}$ plane to be the most plausible K_2 plane (*SI Appendix*, Fig. S2), largely because the experimentally measured twinning shear in Ti and Zr closely matches the value with this plane (12). In contrast, our in situ atomic-scale observations unambiguously show that the operative K_2 plane is the (0001) basal plane, and that the nominal twinning shear exceeds 1.0, previously thought "impossible." Although an analysis for alternative K_2 planes and static atomic-scale observations suggest highly complex atomic shuffles (21), the underlying energetic origin of the alternative twinning mode has remained unresolved. To address this discrepancy, we perform an energetic analysis to explain why the experimentally observed K_2 plane, despite appearing least favorable under classical criteria, is the preferred choice for this twinning mode.

Fig. 2 and *SI Appendix*, Fig. S3 further indicate that the b_3 TD corresponds to a zonal TD comprising shear on three consecutive $\{11\bar{2}2\}$ twinning planes. Our analysis extends the concept of "generalized planar fault energy" (GPFE) (22–24). In this framework, a twin in an HCP crystal is treated as a stack of planar stacking faults on consecutive close-packed planes, where each stacking fault is generated by homogeneous shear associated with a partial Burgers vector. For the b_3 TD, the total shear is decomposed into three partial Burgers vectors acting on three consecutive $\{11\bar{2}2\}$ planes, each carrying 1/3 of the total the b_3 magnitude on each twinning plane.

Notably, the shear direction of the b_1 and the b_3 TDs are opposite, if the designation of "twin" and "matrix" is ignored. This motivates evaluation of the full energy landscape along the $\frac{1}{3}\langle 11\bar{2}3\rangle$ direction, corresponding to a full pyramidal dislocation. The resulting energy profile is shown in Fig. 3*A*. The curve exhibits two distinct peaks: a smaller peak corresponding to homogeneous shear along the b_1 TD, and a much larger peak associated with shear in the opposite direction corresponding to the b_3 TD. Because the b_3 TD involves shear on three consecutive twinning planes, we further calculated the energy profile for each individual plane, as shown in Fig. 3*B*. While the first shear stress for the b_3 TD has a relatively low energy barrier, the second and the third shear encounter substantially higher energy barriers. This result demonstrates that the b_3 TD is energetically unfavorable despite its small nominal shear.

By contrast, although the b_1 TD produces a nominal shear greater than 1.0, its associated energy barrier is significantly lower than that of the b_3 TD. This energetic preference is consistent with the mobility observed in our atomistic simulations (*SI Appendix*, Fig. S4). The constructed b_3 TD remains immobile under increasing applied shear strain, whereas the b_1 TD is highly mobile, and ultimately glides out to the free surface.

The above theoretical analysis indicates that, independent of loading direction, b_3 intrinsically has a lower mobility relative to b_1. While the loading direction dependence exists in principle, the actual twinning behavior may also be influenced by crystal sizes (8, 25), surface energy (26), and composition (27). Notably, surface energy minimization also governs twinning behavior in HCP nanocrystals (26). In stark contrast to the new twinning mode, the (0001) basal plane will transition into the $\{11\bar{2}1\}$ plane for the conventional $\{11\bar{2}2\}$ twin mode, and lead to the higher surface energy (3.77 J/m^2 for (0001) plane, and 4.43 J/m^2 for $\{11\bar{2}1\}$ plane in Re) (28). For all the other options of K_2 (Fig. 2*G*), the preexisting low-energy basal surface also must transform into high-index facets during twinning and substantially raise the surface energy. Therefore, it is energetically favorable that the surface basal plane is the K_2 plane during the twinning process in nanocrystals.

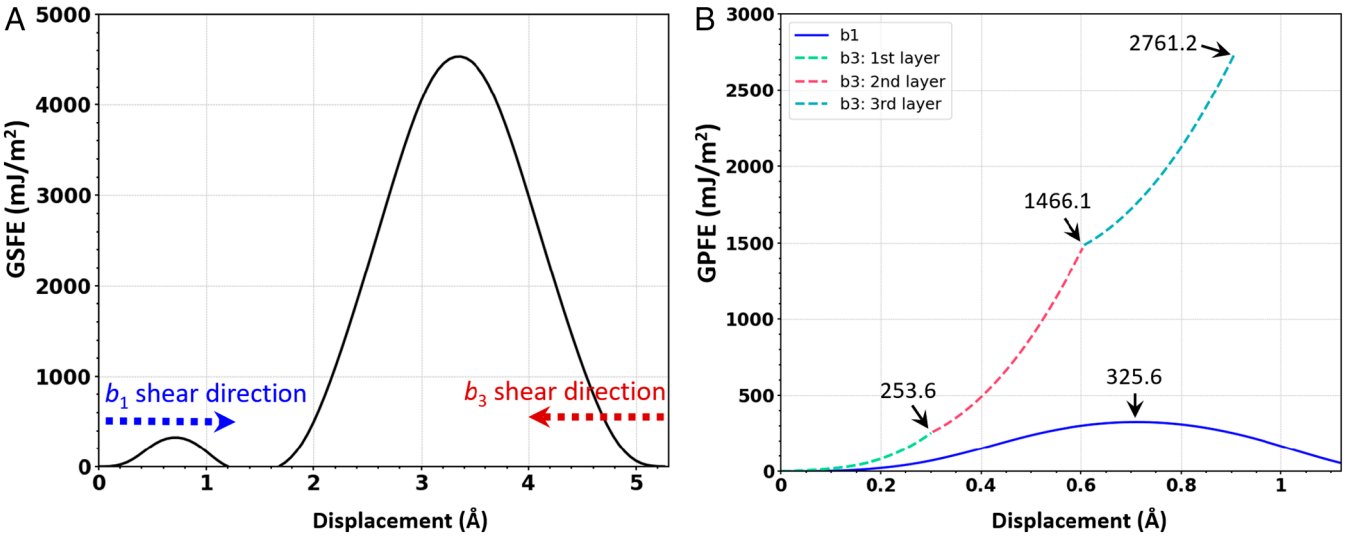

Fig. 3. Modeling of twinning shear. (*A*) GPFE profiles when twinning shear is along the b_1 and b_3 twinning Burgers vectors. Shearing along the b_3 direction encounters a much higher energy barrier, and no metastable state exists along the shear path. (*B*) Comparison of the GPFE for shear along b_1 (the blue curve) and b_3 (the dashed curve). For the b_3 case, the GPFE was calculated by the same amount of shear on three consecutive $\{11\bar{2}2\}$ twinning planes, corresponding to a three-layer zonal twinning dislocation (see b_3 in Fig. 2). The energy barrier for the b_3 configuration is prohibitively high.

Although the $\{11\bar{2}2\}$ twinning mode is favored in nanoscale crystals, it may also be activated in bulk HCP metals through a double twinning mechanism. Fig. 4 shows the process of sequential $\{11\bar{2}1\}$ twinning, leading to the emergence of a $\{11\bar{2}2\}$ twin (29). As shown in Fig. 4 *A*–*C*, tensile loading leads to the formation of the first $\{11\bar{2}1\}$ twin, rotating the basal plane of the matrix by about

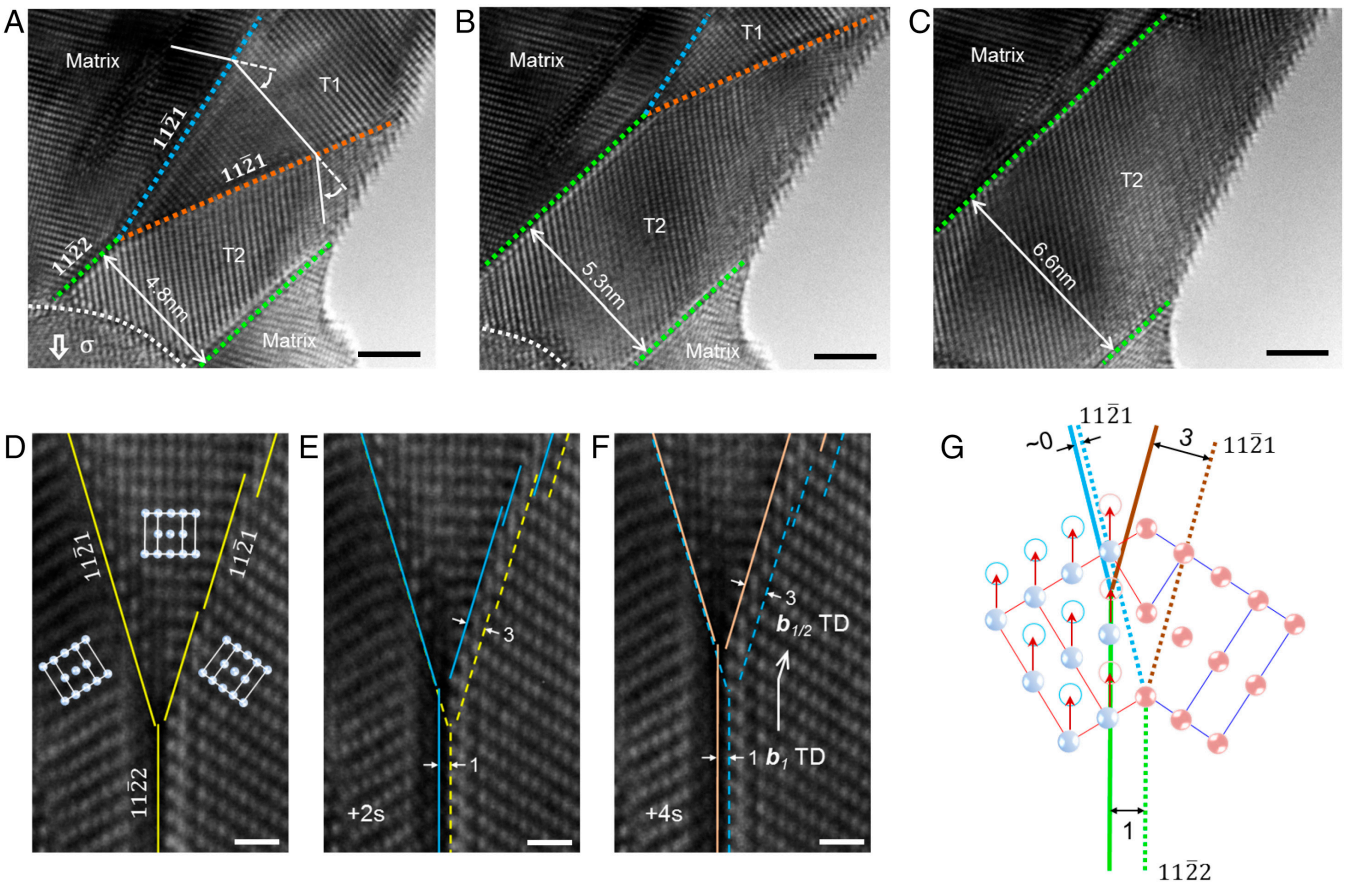

Fig. 4. In situ atomic-resolution observation of $\{11\bar{2}2\}$ twinning through a double twinning process. (*A*–*C*) HRTEM snapshots showing the formation of a $\{11\bar{2}2\}$ twin (marked as T2) through two sequential $\{11\bar{2}1\}$ twinning events (T1) in a $[1\bar{1}00]$-oriented Re nanocrystal under tensile straining approximately along the <*c*> axis. White lines and arrows indicate the progressive rotation of the basal (K_2) planes across the twin boundaries. Note that the basal plane is the K_2 plane for both $\{11\bar{2}1\}$ and $\{11\bar{2}2\}$ twinning. (*D*–*F*) The sequence of double twinning leads to a threefold twin structure, whose evolution is revealed in the HRTEM snapshots. Insets in (*D*) show HCP unit cells. (*G*) Geometrical analysis of the process in (*D*–*F*), demonstrating that a Burgers vector b_1 TD on the $\{11\bar{2}2\}$ twin plane transforms into three $b_{1/2}$ TDs on the $\{11\bar{2}1\}$ twin plane as it glides through the triple junction. [Scale bar in (*A*–*C*), 2 nm and (*D*–*F*), 500 pm.]

Table 1. Summary of twinning modes and corresponding twinning shear strains in common crystal structures: hexagonal close-packed (HCP), body-centered cubic (BCC), and face-centered cubic (FCC)

Crystal structure	Twinning mode (K1/K2)	Twinning shear (s)	s for Re
HCP	$\{10\bar{1}2\}/\{\bar{1}012\}$	$\lvert\gamma^2-3\rvert/(\gamma\sqrt{3})$	0.14
	$\{10\bar{1}1\}/\{10\bar{1}3\}$	$(4\gamma^2-9)/(4\gamma\sqrt{3})$	0.13
	$\{11\,\bar{2}\,1\}/(0001)$	$1/\gamma$	0.62
	$\{11\bar{2}2\}/\{11\bar{2}4\}$	$2(\gamma^2-2)/(3\gamma)$	0.26
	$\{11\bar{2}2\}/(0001)$	$2/\gamma$	1.23
BCC	$\{\bar{1}12\}/\{11\bar{2}\}$	$1/\sqrt{2}$	–
	Anti-twin	$\sqrt{2}$	–
FCC	$\{111\}/\{11\bar{1}\}$	$1/\sqrt{2}$	–

The parameter γ denotes the c/a ratio of the HCP structure, which is 1.615 for pure Re.

35°. Upon further tensile straining, a second $\{11\bar{2}1\}$ twin forms within the initial one, adding another 35° rotation. Together, these two twinning events result in a cumulative 69° rotation of basal planes, consistent with the crystallographic orientation of a $\{11\bar{2}2\}$ twin. The $\{11\bar{2}2\}$ twin then grows as the second $\{11\bar{2}1\}$ twinning step proceeds (*SI Appendix*, Fig. S5). The transformation of the twin boundaries occurs through the movement of a three-fold twin junction. As shown in Fig. 4 *D–F*, this junction advances upward as the $\{11\bar{2}2\}$ twin (T2) expands and the $\{11\bar{2}1\}$ twin (T1) contracts. This transformation is governed by the twinning geometry, as schematically illustrated in Fig. 4*G*): the TD on the $\{11\bar{2}2\}$ plane decomposes into three TDs on the $\{11\bar{2}1\}$ plane. This process is reversible, as the $\{11\bar{2}2\}$ twin can either absorb or emit $\{11\bar{2}1\}$ twins depending on whether the loading is tensile or compressive. Similar reversible behavior was repeatedly observed (*SI Appendix*, Fig. S5). Moreover, the new twinning mode could be activated during the severe plastic deformation of bulk HCP metals. For instance, nanotwinned titanium with ultrahigh strength and ductility was recently obtained via the multiaxial cryoforging processing (30), where $\{11\bar{2}2\}$ twins, along with $\{10\bar{1}2\}$ twins, are predominant in the nanotwinned structure.

The twinning mode holds strong potential for improving mechanical properties of HCP metals. First, as shown in Table 1, it exhibits the highest twinning shear among all major twinning modes in HCP crystals, which may significantly enhance the deformability of these metals. Second, the conventional $\{11\bar{2}2\}$ twinning is typically detrimental to ductility, as gliding basal dislocations are blocked and transmuted upon encountering the twin boundary (31, 32). In contrast, the new $\{11\bar{2}2\}$ twinning mode only temporarily pin active basal dislocations in the matrix. With assistance of a TD, these basal dislocations can penetrate the twin boundary and reemerge as basal dislocations within the twin (Fig. 5). In this way, the new $\{11\bar{2}2\}$ twinning mode enhances strength without compromising the availability of plastic deformation carriers within the material.

To conclude, we identified a twinning process mode with the largest twinning shear and zero atomic shuffling, offering promising potential to enhance both strength and ductility in Re. Since Re has a similar *c/a* ratio compared with Mg and Ti, the findings may

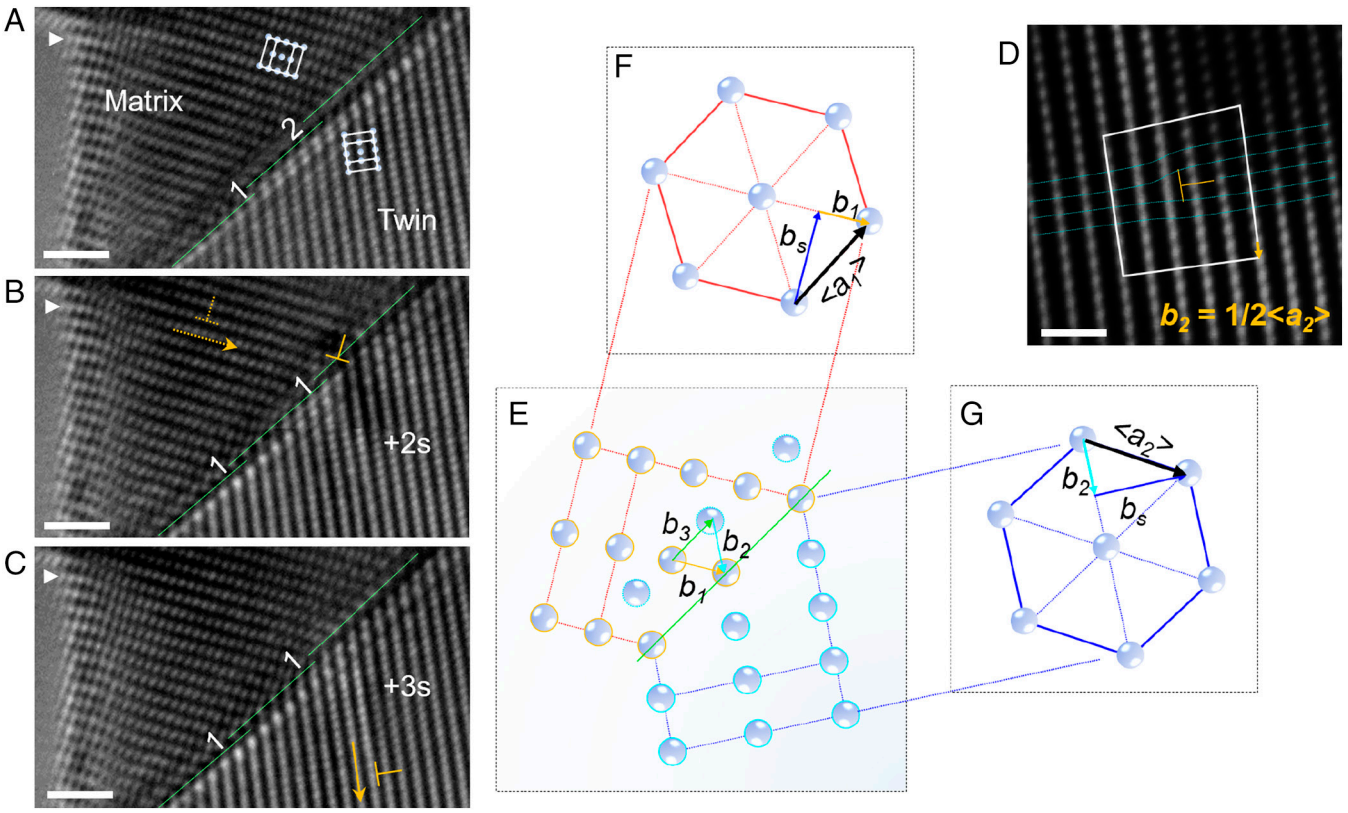

Fig. 5. Interaction of a matrix basal dislocation with the $\{11\bar{2}2\}$ twinning. (*A–C*) Sequential atomic resolution TEM images showing a basal dislocation emission from the side surface, glides in the matrix, stops at the twin boundary, and then keeps gliding as a basal dislocation in the twin. (*D*) Enlarged TEM image of the basal dislocation with illustration of the half-plane feature of the edge dislocation. The white circuit is the Burgers circuit with yellow arrows as the projection of the Burgers vector on the viewing plane. (*E–G*) Topological analysis of the dislocation reactions when the basal dislocation passes through the twin boundary. Note that a twinning dislocation is consumed during this process. [Scale bar in (*A–C*), 1 nm and (*D*), 500 pm.]

be broadly applied in these critical HCP metals which warrants further exploration. More fundamentally, this finding indicates that reducing crystal size can induce unconventional, high-shear twinning modes wherein minimal atomic shuffles are preferred over minimal twinning shear, markedly different from those in bulk crystals. This finding points to a potentially another profound shift in deformation mechanisms in materials with decreasing sizes (10, 19, 33).

Methods

In Situ HRTEM. Rhenium (Re) is widely used as a structure material in jet engines (34), due to its outstanding mechanical properties and excellent oxidation resistances at high temperatures. Moreover, it is resistant to electron irradiation (35), making it a suitable model material for in situ TEM investigations. Re rods with 99.999% purity (*ESPI* metals) were used in this study. The rods were rinsed in acetone and then cleaned in a plasma cleaner to remove surface organic contaminants. Then, they were fractured and loaded onto both the fixed-end and the piezo-end of the Nanofactory TEM-STM holder. Note that when the Re rod was fractured, many nanotips or burrs formed on the fractured surface. The nanotips were then brought into contact and melt-quenched using an electrical pulse to form defect-free nanocrystals inside the high vacuum (~10^{-8} mbar) of the TEM. Mechanical deformation was applied by tensile straining at a controlled rate of 10^{-3} to 10^{-4} /s. All in situ HRTEM experiments were conducted using an FEI 80–300 Titan microscopy equipped with a spherical aberration corrected imaging lens. A charge-coupled device (CCD) camera was used to record images and videos at a rate of 2 frames per second.

Simulation. The embedded atom method (EAM) (36) potential for Re-W binary system developed by Setyawan et al. (37) was employed for the simulations in this study. Within the EAM formalism, the total energy of the system is written as $E_{total} = \sum_i F_i(\bar{\rho}_i) + \frac{1}{2}\sum_{i\neq j}\varphi_{ij}(r_{ij})$, where the host electron density at atom i is $\bar{\rho}_i = \sum_{j\neq i} f_j(r_{ij})$. Here F_i is the embedding energy, φ_{ij} is the pair potential between atoms i and j separated by r_{ij}, and $f_j(r_{ij})$ is the electron density contributed by atom j at the site of atom i. Atomistic simulations were performed using the Large-scale Atomic/Molecular Massively Parallel Simulator (LAMMPS) (38). Atomsk (39) was used to construct the twin crystals. An edge b_1 twinning dislocation was constructed by inserting a dislocation at the twin boundary. For the b_3 zonal twinning dislocation that contains three $\{11\bar{2}2\}$ planes, atomic layers were selectively removed from both the parent and twin to form a three-layer step. Both b_1 and b_3 configurations were relaxed at 300 K for 230 ps using the NVT ensemble (40). The system contains approximately 1.5 million atoms within a simulation cell of dimensions 25 × 30 × 30 nm^3. Free surfaces were applied in all three directions. To study the gliding behaviors of b_1 and b_3 twinning dislocations, atoms in the top and bottom four atomic layers were fixed. A shear strain was generated by displacing the top fixed region along the $[1\bar{2}13]$ twinning direction at a constant rate of 0.1Å/ps, corresponding to a strain rate of 3.39 × 10^8 s^{-1}. To visualize the dislocation line, von Mises stresses were calculated and the data were used to highlight atoms at the dislocation core. OVITO (41) was used to display the simulation results. Common neighbor analysis (CNA) (42) was also used to identify crystal structure and lattice defects.

Data, Materials, and Software Availability. Study data are included in the article and/or *SI Appendix*.

ACKNOWLEDGMENTS. S.X.M. acknowledges support from the NSF (DMR 1808046) through the University of Pittsburgh. C.W. was supported by the PNNL LDRD program. This work was performed, in part, at the William R. Wiley Environmental Molecular Sciences Laboratory, a national scientific user facility sponsored by U.S. Department of Energy, Office of Biological and Environmental Research and located at PNNL. PNNL is operated by Battelle for the US Department of Energy under contract DE-AC05-76RLO1830. B.L. thank the support from National Science Foundation (DMR-2528624).

1. L. Lu, X. Chen, X. Huang, K. Lu, Revealing the maximum strength in nanotwinned copper. *Science* **323**, 607–610 (2009).
2. H. Fu *et al.*, Achieving high strength and ductility in magnesium alloys via densely hierarchical double contraction nanotwins. *Nano Lett.* **17**, 6117–6124 (2017).
3. D. Jang, X. Li, H. Gao, J. R. Greer, Deformation mechanisms in nanotwinned metal nanopillars. *Nat. Nanotechnol.* **7**, 594–601 (2012).
4. L. Li, C. Ortiz, Pervasive nanoscale deformation twinning as a catalyst for efficient energy dissipation in a bioceramic armour. *Nat. Mater.* **13**, 501–507 (2014).
5. J. W. Christian, S. Mahajan, Deformation twinning. *Prog. Mater. Sci.* **39**, 1–157 (1995).
6. X. L. Wu *et al.*, New deformation twinning mechanism generates zero macroscopic strain in nanocrystalline metals. *Phys. Rev. Lett.* **100**, 095701 (2008).
7. H. Zheng, J. Wang, J. Y. Huang, Z. Zhang, S. X. Mao, Dynamic process of phase transition from wurtzite to zinc blende structure in InAs nanowires. *Nano Lett.* **13**, 6023–6027 (2013).
8. Y. He, B. Li, C. M. Wang, S. X. Mao, Direct observation of dual-step twinning nucleation in hexagonal close-packed crystals. *Nat. Commun.* **11**, 2483 (2020).
9. Y. Guo, J. Schwiedrzik, J. Michler, X. Maeder, On the nucleation and growth of 11–22 twin in commercial purity titanium: In situ investigation of the local stress field and dislocation density distribution. *Acta Mater.* **120**, 292–301 (2016).
10. M. D. Uchic, D. M. Dimiduk, J. N. Florando, W. D. Nix, Sample dimensions influence strength and crystal plasticity. *Science* **305**, 986–989 (2004).
11. T. Zhu, L. Ju, A. Samanta, A. Leach, K. Gall, Temperature and strain-rate dependence of surface dislocation nucleation. *Phys. Rev. Lett.* **100**, 025502 (2008).
12. E. J. Rapperport, Room temperature deformation process in zirconium. *Acta Mater.* **7**, 254–260 (1959).
13. W. A. Backofen, N. E. Paton, Plastic deformation of titanium at elevated temperatures. *Metall. Trans. A* **1**, 2839–2847 (1970).
14. B. Li, Shear and shuffle in {11-22}<11-2-3> twinning in titanium. *J. Mater. Res.* **30**, 3795–3802 (2015).
15. B. A. Bilby, A. G. Crocker, The theory of the crystallography of deformation twinning. *Proc. R. Soc. Lond. A Math. Phys. Sci.* **288**, 240–255 (1965).
16. A. Serra, D. J. Bacon, R. C. Pond, The crystallography and core structure of twinning dislocations in H.C.P. metals. *Acta Metall.* **36**, 3183–3203 (1988).
17. A. Serra, R. C. Pond, D. J. Bacon, Computer simulation of the structure and mobility of twinning disclocations in H.C.P. metals. *Acta Metall. Mater.* **39**, 1469–1480 (1991).
18. A. Serra *et al.*, Horstemeyer 'Extended zonal dislocations mediating twinning in titanium'. *Philos. Mag.* **93**, 3495–3503 (2013).
19. B. Y. Liu *et al.*, Large plasticity in magnesium mediated by pyramidal dislocations. *Science* **365**, 73–75 (2019).
20. Z. W. Shan, R. K. Mishra, S. A. Syed Asif, O. L. Warren, A. M. Minor, Mechanical annealing and source-limited deformation in submicrometre-diameter Ni crystals. *Nat. Mater.* **7**, 115–119 (2008).
21. J. Li, M. L. Sui, B. Li, A half-shear-half-shuffle mechanism and the single-layer twinning dislocation for {11-22}<11-2-3>mode in hexagonal close-packed titanium. *Acta Mater.* **216**, 117150 (2021).
22. V. Vitek, Intrinsic stacking faults in body-centered cubic crystals. *Philo. Mag.* **18**, 773–786 (1968).
23. D. H. Warner, W. A. Curtin, S. Qu, Rate dependence of crack-tip processes predicts twinning trends in f.c.c. metals. *Nat. Mater.* **6**, 876–881 (2007).
24. E. B. Tadmor, N. Bernstein, A first-principles measure for the twinnability of FCC metals. *J. Mech. Phys. Solids* **52**, 2507–2519 (2004).
25. L. Wang *et al.*, In situ atomistic deformation mechanisms of twin-structured nanocrystal Pt. *Scripta Mater.* **147**, 103–107 (2018).
26. Y. He, Z. Fang, C. Wang, G. Wang, S. X. Mao, In situ observation of the atomic shuffles during the 11–21 twinning in hexagonal close-packed rhenium. *Nat. Commun.* **15**, 2994 (2024).
27. C. Yang *et al.*, Chemical inhomogeneity-induced profuse nanotwinning and phase transformation in AuCu nanowires. *Nat. Commun.* **14**, 5750 (2023).
28. J. M. Zhang, D. D. Wang, K. W. Xu, Calculation of the surface energy of hcp metals by using the modified embeded atom method. *Appl. Surf. Sci.* **253**, 2018–2024 (2006).
29. A. G. Crocker, Double twinning. *Philos. Mag.* **7**, 1901–1924 (1962).
30. S. Zhao *et al.*, Cryoforged nanotwinned titanium with ultrahigh strength and ductility. *Science* **373**, 1363–1368 (2021).
31. H. El Kadiri, A. L. Oppedal, A crystal plasticity theory for latent hardening by glide twinning through dislocation transmutation and twin accommodation effects. *J. Mech. Phys. Solids* **58**, 613–624 (2010).
32. F. Wang, S. R. Agnew, Dislocation transmutation by tension twinning in magnesium alloy AZ31. *Int. J. Plast.* **81**, 63–86 (2016).
33. Q. Yu *et al.*, Strong crystal size effect on deformation twinning. *Nature* **463**, 335–338 (2010).
34. J. C. Carlen, B. D. Bryskin, Rhenium–A unique rare metal. *Mater. Manuf. Processes* **9**, 1087–1104 (1994).
35. R. F. Egerton, P. Li, M. Malac, Radiation damage in the TEM and SEM. *Micron* **35**, 399–409 (2004).
36. M. S. Daw, M. I. Baskes, Embedded-atom method: Derivation and application to impurities, surfaces, and other defects in metals. *Phys. Rev. B* **29**, 6443–6453 (1984).
37. W. Setyawan, N. Gao, R. J. Kurtz, A tungsten-rhenium interatomic potential for point defect studies. *J. Appl. Phys.* **123**, 205102 (2018).
38. D. Dickel, M. Nitol, C. D. Barrett, LAMMPS implementation of rapid artificial neural network derived interatomic potentials. *Comp. Mater. Sci.* **196**, 110481 (2021).
39. P. Hirel, Atomsk: A tool for manipulating and converting atomic data files. *Comput. Phys. Commun.* **197**, 212–219 (2015).
40. D. J. Evans, B. L. Holian, The Nose-Hoover thermostat. *J. Chem. Phys.* **83**, 4069–4074 (1985).
41. A. Stukowski, Visualization and analysis of atomistic simulation data with OVITO-the Open Visualization Tool. *Modelling Simul. Mater. Sci. Eng.* **18**, 015012 (2010).
42. J. D. Honeycutt, H. C. Andersen, Molecular dynamics study of melting and freezing of small Lennard-Jones clusters. *J. Phys. Chem.* **91**, 4950–4963 (1987).